Spin waves and magnetic Hamiltonian in the low temperature phase of $LiInCr_4O_8$ – Supplementary Material –

Gøran J. Nilsen,[1,2] Rafał Wawrzyńczak,[3,4] Harald O. Jeschke,[5] Hannu Mutka,[3] Takatsugu Masuda,[6] Nicola Casati,[7] Vladimir Pomjakushin,[8] Zenji Hiroi,[6] and Yoshihiko Okamoto[6]

[1]*ISIS Neutron and Muon Source, Science and Technology Facilities Council, Didcot OX11 0QX, United Kingdom*
[2]*Department of Mathematics and Physics, University of Stavanger, 4036 Stavanger, Norway*
[3]*Institut Laue-Langevin, CS 20156, Cedex 9, 38042 Grenoble, France*
[4]*Max Planck Institute for Chemical Physics of Solids, 01187 Dresden, Germany*
[5]*Research Institute for Interdisciplinary Science, Okayama University, Okayama 700-8530, Japan*
[6]*Institute for Solid State Physics, University of Tokyo, Kashiwa, Chiba 277-8581, Japan*
[7]*Swiss Light Source, Paul Scherrer Institute, 5232 Villigen PSI, Switzerland*
[8]*SINQ, Paul Scherrer Institute, 5232 Villigen PSI, Switzerland*

(Dated: March 3, 2025)

I. STRUCTURAL PHASE TRANSITION IN $LIINCR_4O_8$ FROM X-RAY DIFFRACTION.

In order to investigate the symmetry of the low temperature structure with higher precision than afforded by our previous neutron diffraction work [1], we carried out synchrotron X-ray diffraction on the MS-X04A beamline at the Swiss Light Source (PSI, Switzerland) [2]. The sample was loaded in a silica capillary and cooled to 6 K using a side-loading cryostat. Powder diffraction patterns were collected in the temperature range between 6 K and 25 K using an X-ray energy of 22 keV ($\lambda = 0.5635$ Å) and a wide-angle detector spanning $2\theta = 2$ to 85 degrees. In our previous study [3], we analyzed the temperature-dependence of the (800) reflection, which exhibits a large splitting upon cooling below the structural transition at $T_u = 17$ K. For the purpose of comparison, we therefore show the temperature dependence of the same peak from the current dataset on cooling below the structural and magnetic ($T_l = 13$ K) transitions. Fitting the split peak with a sum of three Voigt functions showed that the observed splitting is fully accounted for by two reflections from the low-temperature phase and one from the high-temperature cubic $F\bar{4}3m$ phase, which persists at low temperature (Fig. S1). This shows that the symmetry of the low-temperature phase is (within the resolution) at most tetragonal.

Fitting the entire pattern to the previously assigned $I\bar{4}m2$ space group, an adequate description of the whole pattern is achieved (see Fig. S2), with no diffraction peaks not indexed (aside from those due to the Cr_2O_3 impurity phase). The remaining deviation between experiment and refinement is due to the complex line-shape of the diffraction peaks, which are broadened not only due to resolution, but also finite particle size and strain. The parameters of the synchrotron XRD data are shown in Table S1.

To complement the X-ray diffraction above, and to study the temperature dependence of the atomic displacements in more detail, additional neutron diffraction measurements were performed on the HRPT instrument, also at PSI. Neutron wavelengths of 1.494 Å and 1.886 Å were selected by the (335) and (115) reflections of a Ge monochromator at a takeoff angle of $2\theta_M = 120°$. The parameters resulting from Rietveld refinement to the base temperature (2 K) data are shown in Table S2: generally, they are in good agreement with the synchrotron x-ray data. The full temperature-dependence will be reported elsewhere.

II. ADDITIONAL INFORMATION ABOUT DFT ENERGY MAPPING

The density functional theory (DFT) based energy mapping approach uses DFT total energies of a large number of different spin configurations to exctract the relevant parameters of the Heisenberg Hamiltonian. We study the Hamiltonian

$$H = \sum_{i<j} J_{ij} \mathbf{S}_i \cdot \mathbf{S}_j \,, \tag{1}$$

where the sum runs over pairs of spins on the distorted pyrochlore lattice. The spins of the Cr^{3+} magnetic sites are to very good approximation $S = 3/2$. We perform the calculations on the powder X-ray diffraction structure obtained by TOPAS as described in the main text (see Table I of the main text). In order to resolve a sufficient number of exchange interactions, we create a 5-fold supercell of the primitive cell of the structure with $I\bar{4}m2$ space group. This contains 20 symmetry inequivalent Cr^{3+} sites that allows for more than 50000 magnetic patterns with distinct energies. This allows us to resolve 21 exchange interactions up to a Cu-Cu distance of 8.78 Å which is about three times the nearest neighbor Cu-Cu distance of $LiInCr_4O_8$. This is useful for confirming that indeed the four shortest bonds J_1 to J_4 which derive from J and J' in the high temperature cubic structure are by far the most important interactions. The energy scale of the Heisenberg Hamiltonian parameters is not fixed by the DFT calculations as every choice of the on-site interaction strength U leads to a different overall energy scale. We determine the energy scale by demanding that the final result matches the high temperature Curie-Weiss behavior of the material as given by the Curie-Weiss temperature $\theta_{\rm CW} = -332$ K [4]. We use $\theta_{\rm CW}$ to fix the on-site interaction U while we keep the Hund's rule coupling fixed at the literature value $J_{\rm H} = 0.72$ eV [5]. We find a value of $U = 2.64$ eV as indicated by a vertical line in Fig. 2 of the main text. The full set of couplings at this U value is $J_1 = 75.0(3)$ K, $J_2 = 34.4(3)$ K, $J_3 = 20.8(1)$ K,

$J_4 = 7.8(3)$ K, $J_5 = 1.5(3)$ K, $J_6 = -0.6(2)$ K, $J_7 = 1.3(3)$ K, $J_{8a} = 2.8(2)$ K, $J_{8b} = 2.5(2)$ K, $J_{9a} = 0.7(2)$ K, $J_{10} = 1.4(3)$ K, $J_{11} = -1.6(3)$ K, $J_{12} = 1.1(3)$ K, $J_{13} = 0.4(2)$ K, $J_{14} = 0.3(1)$ K, $J_{16} = 1.3(3)$ K, $J_{17} = 1.3(2)$ K, $J_{18} = -0.7(2)$ K, $J_{19} = 0.0(1)$ K, $J_{20} = 0.0(1)$ K, $J_{23} = 1.4(3)$ K. In Fig. S3, we show that the quality of the fit we achieve is nearly perfect. Table S3 contains the calculated results for eight different values of the onsite interaction strength U.

III. ADDITIONAL LINEAR SPIN WAVE THEORY RESULTS

Linear spin wave theory was carried out using the `SpinW` package [6]. Initial attempts at global optimization of the model parameters to the experimental $S(|Q|, \Delta E)$ using simulated annealing and particle swarm algorithms (we note that methods based on the calculation of gradients are not efficient due to the noise in χ^2 generated by the sampling inherent to the powder averaging algorithm) yielded several solutions with similar $\chi^2 = [S(|Q|, \Delta E)_{\text{obs}} - S(|Q|, \Delta E)_{\text{calc}}]^2$. To more effectively map these minima in the parameter space of the model, the optimization was instead performed by constructing a $10\times10\times10\times10$ grid in the four main exchange parameters J_{1-4}, subject to the constraints that $J_1 > J_2$ and $J_3 > J_4$ as required by the experimentally observed magnetic structure, as well as $J_1 > J_3$, as indicated by the DFT calculations. The overall energy scale was set by J_1, which was allowed to vary between 0.1 and 10 meV. $S(|Q|, \omega)$ was calculated for 5 diagnostic cuts at fixed values of $|Q|$: 1.1, 1.5, 1.7, 2.0, and 2.2Å^{-1} with $\Delta Q = 0.2$Å^{-1}. An initial χ^2 was calculated after first optimizing the amplitude and a flat background, then a local optimization of all the model parameters was performed for the 16 solutions found below a threshold value of $\chi^2 < 2$. The $S(|Q|, \Delta E)$ calculated from the optimized parameters generated by this method are shown in Figure S4 and the parameters and χ^2 are listed in Table S4. The χ^2 were found to range between 1.53 and 1.95.

Relationships between the parameters were sought by calculating parameter ratios for all solutions, then ratios of linear combinations of all pairs of parameters. It was thus found that the ratio $(J_1 + J_4)/(J_2 + J_3)$ was approximately constant across all parameters sets (see S4), with the only significant deviations coming from the solutions with the highest χ^2.

Finally, the residual frustration in the low-temperature short-range ordered state is indicated by a dispersionless zero-energy mode along the $X - X'$ direction in the Brillouin zone (corresponding to the c direction in the crystallographic cell) for all sets of J_{1-4} determined above (Fig. S5). This degeneracy is not lifted by further neighbor interactions up to J_8 assuming that the low-temperature state is collinear. It must then be small deviations from collinearity combined with possible higher order (e.g. Dzyaloshinskii-Moriya) or longer-ranged interactions that stabilize the low-temperature state. It was not possible to quantify these from the current data.

[1] G. J. Nilsen, Y. Okamoto, T. Masuda, J. Rodriguez-Carvajal, H. Mutka, T. Hansen, and Z. Hiroi, Complex magnetostructural order in the frustrated spinel $LiInCr_4O_8$, Phys. Rev. B **91**, 174435 (2015).

[2] P. R. Willmott, D. Meister, S. J. Leake, M. Lange, A. Bergamaschi, M. Böge, M. Calvi, C. Cancellieri, N. Casati, A. Cervellino, Q. Chen, C. David, U. Flechsig, F. Gozzo, B. Henrich, S. Jäggi-Spielmann, B. Jakob, I. Kalichava, P. Karvinen, J. Krempasky, A. Lüdeke, R. Lüscher, S. Maag, C. Quitmann, M. L. Reinle-Schmitt, T. Schmidt, B. Schmitt, A. Streun, I. Vartiainen, M. Vitins, X. Wang, and R. Wullschleger, The materials science beamline upgrade at the Swiss Light Source, J. Synchrotron Rad. **20**, 667 (2013).

[3] G. Nilsen, T. C. Hansen, Z. Hiroi, T. Masuda, H. Mutka, Y. Okamoto, and C. Tassel, Magnetostructural coupling and spin dynamics in the 'breathing' pyrochlore antiferromagnets liincr4o8 and ligacr4o8 (2013).

[4] Y. Okamoto, G. J. Nilsen, J. P. Attfield, and Z. Hiroi, Breathing pyrochlore lattice realized in A-site ordered spinel oxides $LiGaCr_4O_8$ and $LiInCr_4O_8$, Phys. Rev. Lett. **110**, 097203 (2013).

[5] T. Mizokawa and A. Fujimori, Electronic structure and orbital ordering in perovskite-type 3d transition-metal oxides studied by hartree-fock band-structure calculations, Phys. Rev. B **54**, 5368 (1996).

[6] S. Toth and B. Lake, Linear spin wave theory for single-q incommensurate magnetic structures, Journal of Physics: Condensed Matter **27**, 166002 (2015).

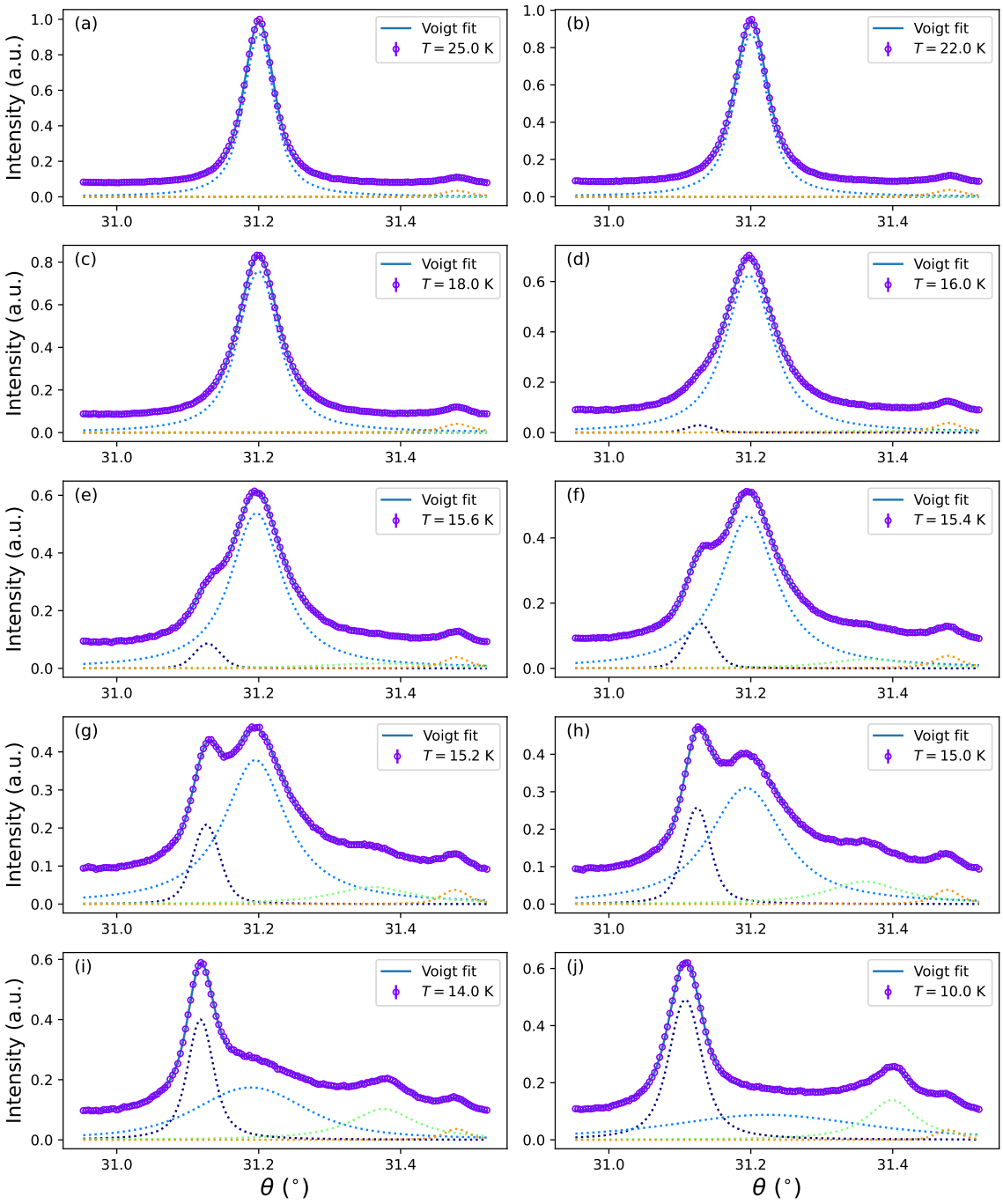

FIG. S1. Simultaneous Voigt profile fits to synchrotron X-ray powder diffraction (800) peak of the high temperature cubic phase of $LiInCr_4O_8$ and two peaks associated with tetragonal phase emerging below the structural transition at T_u. Small additional peaks on the high angle side of (800) are present at all temperatures and result from a Cr_2O_3 impurity phase.

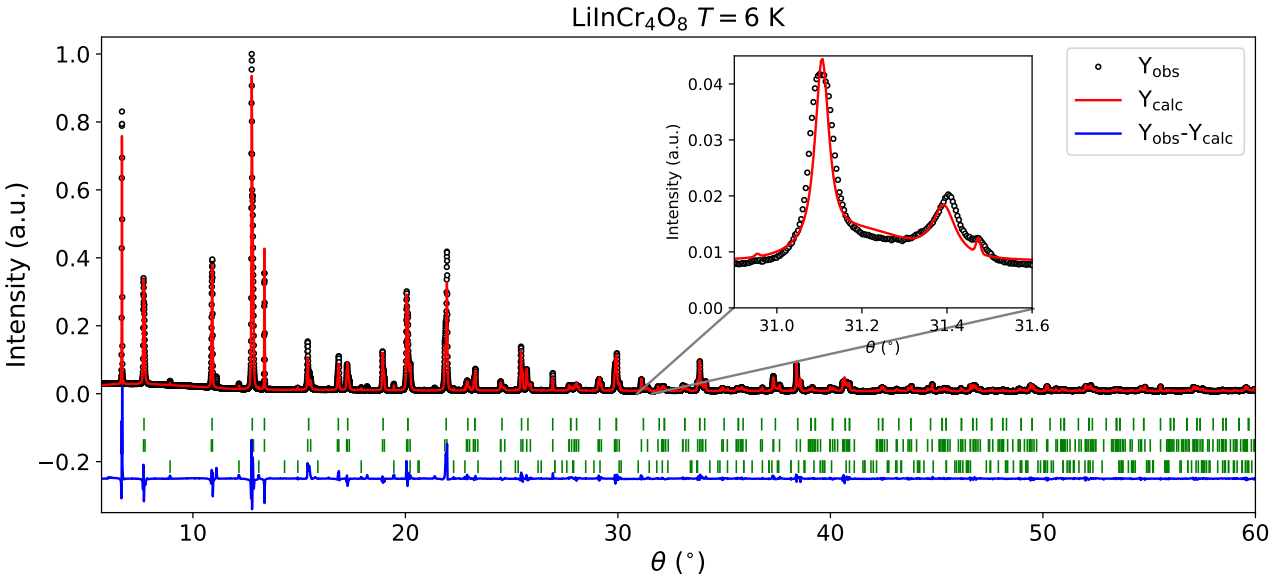

FIG. S2. Rietveld refinement of SXRPD data collected on $LiInCr_4O_8$, as described in the main text, at $T = 6$ K. The refinement assumed two phases, namely the high temperature cubic $F\bar{4}3m$ and low temperature tetragonal $I\bar{4}m2$, and traces of residual Cr_2O_3 impurity phase. Green markers show the predicted positions of Bragg reflections of listed phases (top to bottom in order of listing). The inset shows a magnification of the region around the (800) peak. The deviations between the model and data are primarily due to the difficulty of modeling the complex line-shape, a convolution of the instrumental resolution and both particle size and strain broadening.

TABLE S1. Structural parameters of the $F\bar{4}3m$ and $I\bar{4}m2$ model for $LiInCr_4O_8$, refined from SXRPD data (fig. S2), collected as described in the main text. Agreement factors: $\chi^2 = 3.88$, $R_p = 8.34$, $R_{wp} = 9.18$.

	$F\bar{4}3m$					$I\bar{4}m2$				
Atom	x	y	z	B (Å^{-2})	Wyck.	x	y	z	B (Å^{-2})	Wyck.
^{7}Li	0.00000	0.00000	0.00000	0.1(2)	4a	0.00000	0.00000	0.00000	0.1(2)	2a
In	0.75000	0.75000	0.75000	0.290(8)	4d	0.00000	0.50000	0.75000	0.290(8)	2d
Cr	0.3714(1)	0.3714(1)	0.3714(1)	0.193(9)	16e	0.00000	0.7431(3)	0.3705(2)	0.193(9)	8i
O1	0.1403(4)	0.1403(4)	0.1403(4)	0.56(3)	16e	0.00000	0.265(1)	0.1332(7)	0.56(3)	8i
O2	0.6209(5)	0.6209(5)	0.6209(5)	0.56(3)	16e	0.00000	0.2129(6)	0.6067(6)	0.56(3)	8i

TABLE S2. Structural parameters of the $I\bar{4}m2$ model refined from neutron powder diffraction data taken with $\lambda = 1.494$ Å and $\lambda = 1.886$ Å at 2 K at HRPT, PSI. Lattice parameters: $a = 5.96162(5)$ Å, $c = 8.3550(1)$ Å. Agreement factors for $\lambda = 1.494$ Å ($\lambda = 1.886$ Å): $\chi^2 = 3.71(2.94)$, $R_p = 8.64(12.9)$, $R_{wp} = 8.64(13.5)$.

Atom	x	y	z	B (Å^{-2})	Wyck.
^{7}Li	0.00000	0.00000	0.00000	0.37(9)	2a
In	0.00000	0.50000	0.75000	0.10(5)	2d
Cr	0.00000	0.746(1)	0.3714(6)	0.37(2)	8i
O1	0.00000	0.2791(6)	0.1354(4)	0.45(1)	8i
O2	0.00000	0.2208(6)	0.6120(3)	0.45(1)	8i

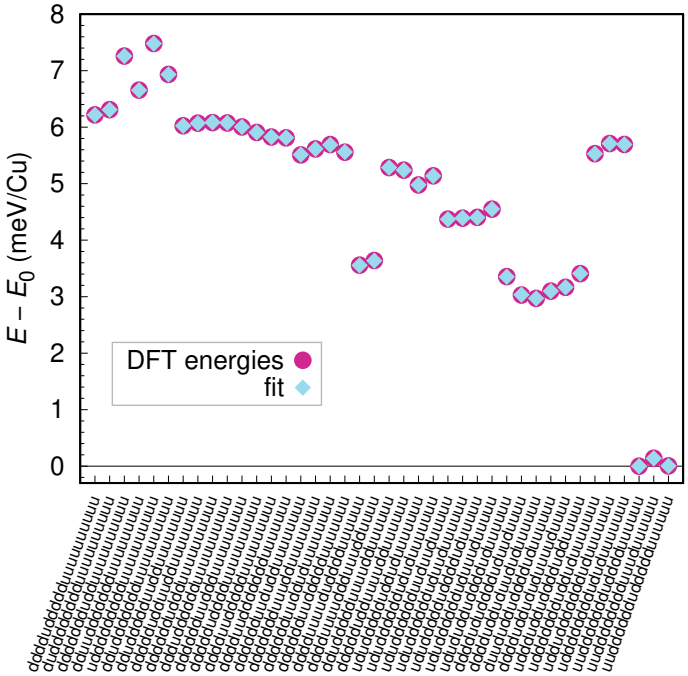

FIG. S3. Comparison between DFT total energies calculated for 40 distinct spin configurations and the fit to the Heisenberg Hamiltonian, Eq. (1). On-site Coulomb strength was $U = 2.5$ eV. The fit is excellent.

TABLE S3. Exchange interactions calculated by DFT energy mapping using the synchrotron X-ray powder diffraction crystal structure tabulated in Table I of the main text. The Hund's rule coupling is set to $J_H = 0.72$ eV. The exchange interactions are identified by the Cu-Cu distances given in the last line. The line in bold face is interpolated and corresponds to the experimental Curie-Weiss temperature $\theta_{CW} = -332$ K as described in the text.

U (eV)	J_1 (K)	J_2 (K)	J_3 (K)	J_4 (K)	J_5 (K)	J_6 (K)	J_7 (K)	J_{8a} (K)	J_{8b} (K)	J_{9a} (K)	$\frac{J_1+J_4}{J_2+J_3}$
1.50	108.3(6)	56.8(6)	33.9(2)	18.7(6)	3.8(5)	-1.5(4)	3.4(6)	5.3(4)	4.9(4)	-0.4(4)	1.4002
1.75	99.8(5)	51.0(5)	30.6(2)	15.8(5)	3.1(4)	-1.2(3)	2.7(5)	4.6(3)	4.2(4)	0.0(3)	1.4167
2.00	92.1(4)	45.8(4)	27.5(2)	13.2(4)	2.5(4)	-1.0(3)	2.2(4)	3.9(3)	3.6(3)	0.3(3)	1.4366
2.25	85.0(4)	41.1(3)	24.7(1)	10.9(3)	2.1(3)	-0.8(2)	1.8(3)	3.4(2)	3.1(3)	0.5(2)	1.4574
2.50	78.4(3)	36.7(3)	22.2(1)	8.9(3)	1.7(3)	-0.7(2)	1.4(3)	3.0(2)	2.7(2)	0.6(2)	1.4822
2.64	**75.0(3)**	**34.4(3)**	**20.8(1)**	**7.8(3)**	**1.5(3)**	**-0.6(2)**	**1.3(3)**	**2.8(2)**	**2.5(2)**	**0.7(2)**	**1.4986**
2.75	72.4(3)	32.7(2)	19.8(1)	6.9(3)	1.4(2)	-0.6(2)	1.2(2)	2.6(2)	2.4(2)	0.7(2)	1.5105
3.00	66.9(2)	29.1(2)	17.5(1)	5.1(2)	1.2(2)	-0.5(2)	0.9(2)	2.4(2)	2.1(2)	0.8(2)	1.5451
3.25	61.8(2)	25.8(2)	15.3(1)	3.4(2)	1.0(2)	-0.4(1)	0.8(2)	2.1(1)	1.8(1)	0.8(2)	1.5864
d_{Cu-Cu} Å	2.86358	2.89906	3.04894	3.05859	5.12161	5.13178	5.15738	5.92199	5.92199	5.948	

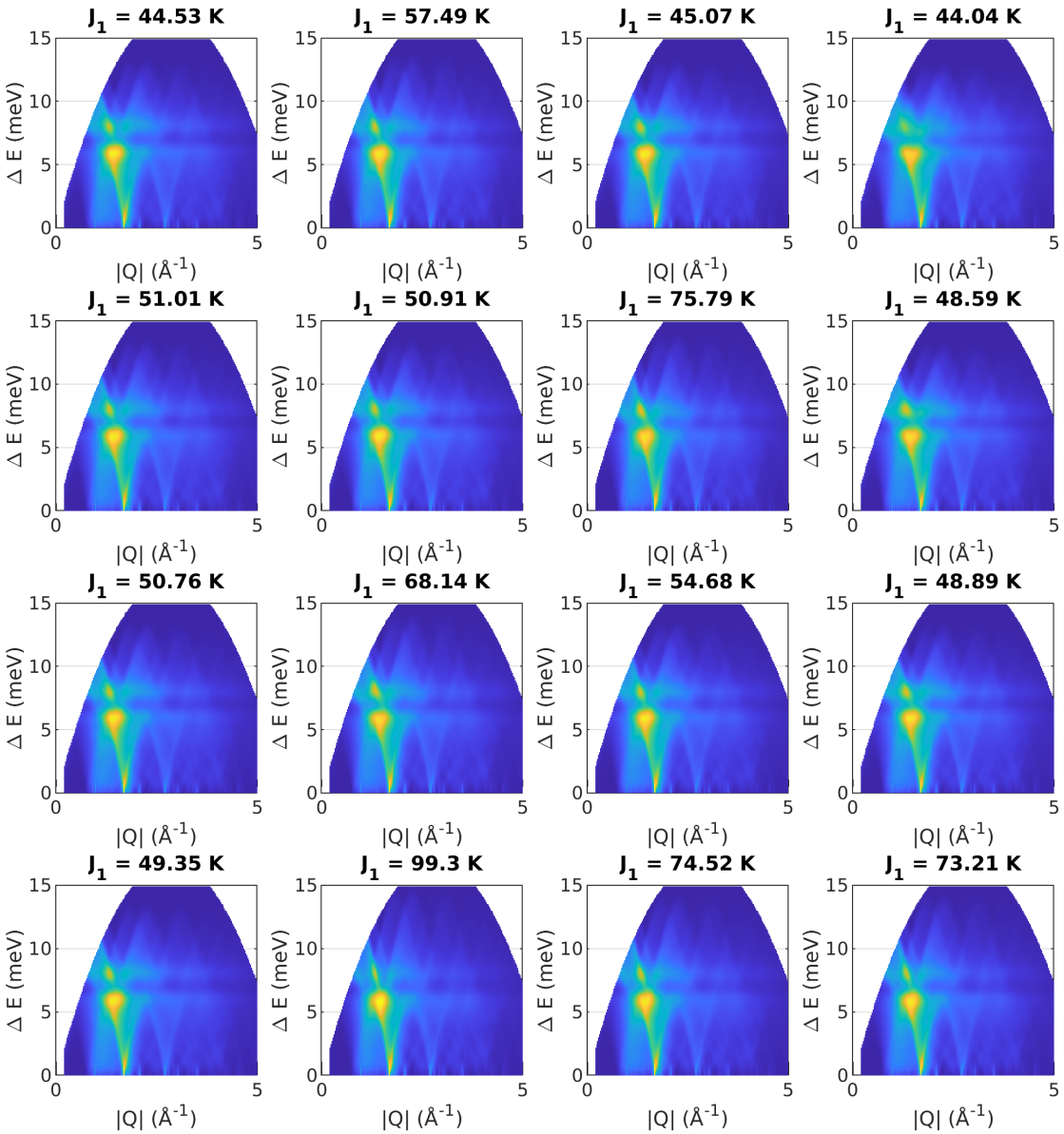

FIG. S4. Calculated $S(|Q|, E = \hbar\omega)$ for the parameters optimised using the 16 best solutions from the grid search described in the text. The full set of parameters and χ^2 are given in Table S4.

TABLE S4. Exchange parameters from local optimizations around the 16 lowest χ^2 points after the grid search of the model parameter space. Note that except for one outlier, the solutions have $(J_1 + J_4)/(J_2 + J_3)$ in the range $[1.1836, 1.2723]$, with a mean of 1.2441 and standard deviation of 0.0228. The only outlier (highlighted in red in the table) has a significantly higher χ^2 than the remaining solutions.

J_1 (K)	J_2 (K)	J_3 (K)	J_4 (K)	$\frac{J_1+J_4}{J_2+J_3}$	χ^2
44.53	24.29	18.56	9.27	1.2556	1.8109
57.49	36.63	15.23	7.85	1.2600	1.6812
45.07	25.04	18.31	8.87	1.2443	1.8121
44.04	26.55	20.74	5.76	1.0530	1.9499
51.01	30.49	16.85	8.51	1.2571	1.7500
50.91	30.12	16.70	8.38	1.2663	1.7550
75.79	54.28	11.97	6.09	1.2360	1.5816
48.59	29.20	17.90	7.17	1.1836	1.8520
50.76	30.16	16.81	8.39	1.2591	1.7484
68.14	47.46	13.95	6.65	1.2178	1.6363
54.68	33.69	15.56	7.97	1.2723	1.7147
48.89	28.72	17.42	8.06	1.2341	1.7810
49.35	28.86	17.37	8.63	1.2541	1.7623
99.30	76.55	9.69	6.01	1.2211	1.5320
74.52	52.72	12.35	6.81	1.2499	1.5410
73.21	51.51	12.77	7.11	1.2495	1.5443

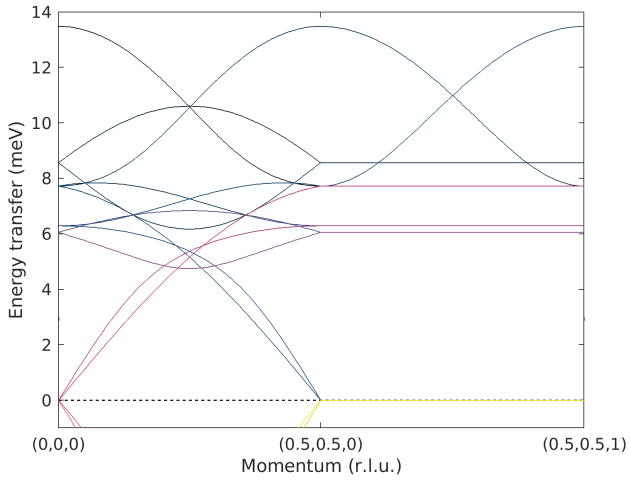

FIG. S5. Linear spin wave dispersion on the $\Gamma - X - X'$ Brillouin zone path for the body-centered tetragonal $I\bar{4}m2$ structure. The magnetic propagation vector corresponds to X. Note the dispersionless zero-energy mode along the (001) direction, which is caused by the decoupling of planes discussed in the main text.